Energy Equip. Sys./ Vol. 8/No. 2/June 2020/ 127-141

ENERGY EQUIPSYS

Energy Equipment and Systems

http://energyequipsys.ut.ac.ir
www.energyequipsys.com

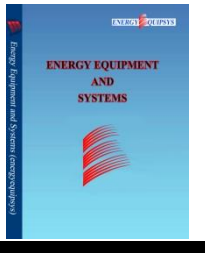

Large eddy simulation of propane combustion in a planar trapped vortex combustor

Authors

Reza Sharifzadeh [a]
Asghar Afshari [a*]

[a] School of Mechanical Engineering, College of Engineering, University of Tehran, North Kargar Avenue, Tehran, 1439957131, Iran

ABSTRACT

Propane combustion in a trapped vortex combustor (TVC) is characterized via large eddy simulation coupled with filtered mass density function. A computational algorithm based on high order finite difference (FD) schemes, is employed to solve the Eulerian filtered compressible Navier-Stokes equations. While, a Lagrangian Monte-Carlo solver based on the filtered mass density function is invoked to describe the scalar field. The impact of injection strategy on temperature distribution and flame structure in a planar single-cavity TVC is investigated. A fuel jet and an air jet are injected directly into the cavity from the forebody and the afterbody, respectively. Different injection schemes are contemplated by altering fuel and air jet locations representing the different flow and flame structures. The temperature distribution, along with cross-sectional averaged temperature and flame structure, are compared for fuel/air injection strategies. The temperature field reveals that configurations in which both air and fuel jets are located at the cavity-walls midpoint or adjacent to the cavity inferior wall, lead to a more uniform temperature distribution and lower maximum temperature with the latter configuration performing slightly better. While, the former configuration provides the closest cross-sectional averaged temperature to the adiabatic flame temperature. The reaction rate distributions show that the configurations mentioned above lead to a more contained flame, chiefly due to more efficient fuel-air mixing at lower regions of the cavity.

Article history:

Received : 21 December 2018
Accepted : 5 March 2019

Keywords: Trapped Vortex Combustor, Large Eddy Simulation, Temperature Distribution, Flame Structure.

1. Introduction

Trapped vortex combustor (TVC), with a vortex trapped in a cavity providing flame stability, has attracted wide interests around the combustion community since 1995. The experimental investigations of Hsu et al. [1] proved that the TVC affords several remarkable advantages such as ignition enhancement, lower emission levels, and extended operating range compared to conventional swirl-stabilized combustors.

The TVC concept invokes a cavity to provide a self-sustaining and continuous source of ignition and flame propagation into the mainstream. Many studies were subsequently concentrated on the TVC concept, chiefly for the applications to gas turbines [2,3]. Due to its exclusive characteristics, trapped vortex combustor has been an interesting topic for combustion researchers, and numerous experimental [1,4–11] and numerical [12–17] investigations have been conducted to shed lights on the different characteristics of this type of flame holder.

* Corresponding author: Asghar Afshari
School of Mechanical Engineering, College of Engineering, University of Tehran, North Kargar Avenue, Tehran, 1439957131, Iran
Email: afsharia@ut.ac.ir

In the TVC configuration, the pilot flame is protected from the mainstream by the cavity and stabilized inside even when the main airspeed is high. Hendricks et al. [2] investigated a laboratory-scale rectangular TVC with an inlet Mach number of 0.7. Their results indicated that with increasing the inlet Mach number, vortices remained trapped within the cavity, and the flame became more intense, more powerful, and shorter due to increment of reaction rate.

Jin et al. [18] experimentally and computationally investigated a laboratory-scale TVC. The experimental tests were conducted for mainstream flow rates comparable to real liquid-fueled aero-engines. Results showed acceptable accordance between PIV measurements and numerical data obtained by RANS simulations. In another study, Zhang and Fan [6] investigated the vortex structure in non-reacting and reacting flows for a trapped-vortex combustor with methane. They reported flow field, vortex structure, and vortex core location within the cavity. Their results indicated that the vortex structure and position is considerably different in reacting and non-reacting flows. The fuel and air need to be introduced directly into the cavity to reinforce the formed pilot flame in a well-designed cavity. Arrangement of fuel and air injectors is still one of the main challenges of cavity flame-holder design.

Recently Kumar and Mishra [19] have conducted a numerical study to investigate the flow structure of a 2D twin trapped vortex combustor. Their results revealed significant differences in the velocity gradient at the shear layer between non-reacting and reacting flow conditions. The reacting flow provides higher levels of turbulent kinetic energy at the cavity zone due to volume expansion arising from combustion.

Krishna and Ravikrishna [8] performed optical diagnostic measurements to investigate the impact of momentum flux ratio (MFR, the ratio of cavity injector to mainstream momentum) on the fuel-air mixing and vortical structure inside the cavity of a single cavity planar TVC. Their results indicate that the MFR parameter plays a significant role in mixing and combustion. The acetone PLIF measurements showed that at high MFRs, the fuel-air mixing quality in the cavity is improved as MFR decreases, due to the modification of vortex structure in the cavity.

The impact of strut length on the characteristics of a TVC was experimentally investigated by Li et al. [20]. Results showed that the longer struts lead to prominent improvements in lean-bow-out and ignition, while the combustion efficiency associated with the shorter struts is higher than long ones. Simulations indicated that weak ignition performance and lean-blow-out limits of the shorter struts raised from an extensive mainstream air entrainment into the cavity and the improved combustion efficiency associated with shorter struts are due to extended wake regions created behind the struts. In another study, Zbeeb [21] investigated the impact of fuel jet Reynolds Number on the emission performance of a two-after-body axisymmetric TVC with syngas fuel. Correlation plots for NOx, CO, and CO2 emissions versus fuel jet Reynolds Number were created.

The first notable investigation of injection location effects on the trapped vortex combustor performance was performed by Ying et al. [22]. In their experimental study, the effect of front-wall-fueling (FWF) and back-wall-fueling (BWF) schemes on the combustion characteristics of a planar TVC was investigated. Their results showed that the BWF scheme with a fuel injection position located farther from the mainstream results in higher combustion efficiency than the FWF scheme with a fuel injection position located closer to the mainstream. In another investigation, Chen et al. [16] studied an axisymmetric miniature ramjet TVC to evaluate the impact of fuel injection location on the fuel-air mixing quality by considering four different fuel injection locations. For the first 3 cases, the fuel is injected directly into the cavity, whereas in the last one at the upstream of the cavity. They concluded that due to the formation of a fuel-rich zone, cases in which fuel is directly injected into the cavity, cannot provide a stable pilot flame while injecting

the fuel into the mainstream increases the mixing efficiency.

Zhao et al. [23] reviewed many aspects of the TVC concept as an alternative configuration for conventional swirl-stabilized combustors. They considered TVC as a multi-physics subject and discussed many characteristics, including cavity/flow aerodynamics and aeroacoustics, fuel-air injection and mixing, emissions, and combustion of alternative fuels. They addressed challenges with the design and implementation of a TVC and mentioned the developments in its industrial applications.

The filtered mass density function (FMDF), is now considered as one of the most efficient tools of employing large eddy simulation (LES) in turbulent reacting flows [24]. Reliability, consistency, and affordability of the hybrid scheme of LES/FMDF are demonstrated for unsteady 3-dimensional simulating of turbulent reacting flows with large-density variations and strong turbulence combustion interactions [25]. Yilmaz et al. [24] overviewed the recent progresses in the simulation of turbulent reacting flows using filtered mass density function. They concluded that recent advances in FMDF simulation include (1) establishment of an irregularly portioned Lagrangian Monte Carlo FMDF solver and (2) implementation of (any) Monte Carlo solver on Eulerian flow fields covered by unstructured grids.

As mentioned before, several studies have been devoted to investigating the impact of different parameters such as Reynolds and Mach numbers, momentum flux ratio, cavity dimensions, and combustor geometry on the combustion performance and flame structure in TVCs. However, only a few studies have focused on the effect of the fueling scheme and arrangements of fuel/air jets. A well-designed injection scheme makes an appropriate fuel-air mixing inside the cavity, leads to more stable combustion, and reduces the flame length and residence times and, thereby, thermal NO_x emission. In the present study, a relative positioning of fuel and air jets entering the cavity is considered to study the effect of fuel and air injection strategy on temperature distribution and flame structure. For this, vortical structure, the variation of cross-sectional averaged temperature and reaction rate distributions are invoked. In brief, the main objective of this study is to identify the best arrangement of fuel-air injection with more efficient combustion. A hybrid Eulerian-Lagrangian solver is employed to achieve this aim. In this scheme, a computational algorithm based on high order finite difference schemes is employed to solve the Eulerian filtered compressible Navier-Stokes equations, while a Lagrangian Monte-Carlo solver is invoked to describe the scalar field. The scheme mentioned above is utilized for the first time in the simulation of TVC-based reacting flows.

2. Theoretical formulation and numerical method

The LES/FMDF scheme solves a hybrid system of Eulerian and Lagrangian equations for capturing the flow and scalar (temperature and mass fractions) variables [25–30]. These equations are given separately in two sections.

2.1. LES governing equations

The set of Favre-filtered LES governing equations for compressible flow represented in the generalized coordinate system are summarized as [25]:

$$\frac{\partial}{\partial t}JU+\frac{\partial \hat{F}}{\partial \xi}+\frac{\partial \hat{G}}{\partial \eta}+\frac{\partial \hat{H}}{\partial \zeta}=J\hat{S} \tag{1}$$

In the above equation, t is the time, ξ, η, ζ are generalized coordinates, and J represents the determinant of the coordinates transformation Jacobian.

$\hat{F}$, $\hat{G}$, and $\hat{H}$ fluxes are given by:

$$\begin{aligned}\hat{F}&=J\big[\xi_t U+\xi_x(F-F_v)+\xi_y(G-G_v)\\&\qquad+\xi_z(H-H_v)\big]\\ \hat{G}&=J\big[\eta_t U+\eta_x(F-F_v)\\&\qquad+\eta_y(G-G_v)\\&\qquad+\eta_z(H-H_v)\big]\\ \hat{H}&=J\big[\zeta_t U+\zeta_x(F-F_v)\\&\qquad+\zeta_y(G-G_v)\\&\qquad+\zeta_z(H-H_v)\big]\end{aligned} \tag{2}$$

In the above equations, F, G, and H indicate the inviscid fluxes, and, F_v, G_v, and H_v denote

the viscous fluxes. And ξ_t, ξ_x, … , ζ_z are the metric coefficients. These fluxes can be represented by the filtered variables as follows:

$$F = \{\bar{\rho}\tilde{u}, \bar{\rho}\tilde{u}^2 + \bar{p}, \bar{\rho}\tilde{u}\tilde{v}, \bar{\rho}\tilde{u}\widetilde{w}, (\bar{\rho}\tilde{E} + \bar{p})\tilde{u}\}$$
$$G = \{\bar{\rho}\tilde{v}, \bar{\rho}\tilde{u}\tilde{v}, \bar{\rho}\tilde{v}^2 + \bar{p}, \bar{\rho}\tilde{v}\widetilde{w}, (\bar{\rho}\tilde{E} + \bar{p})\tilde{v}\} \quad (3)$$
$$H = \{\bar{\rho}\widetilde{w}, \bar{\rho}\tilde{u}\widetilde{w}, \bar{\rho}\tilde{v}\widetilde{w}, \bar{\rho}\widetilde{w}^2 + \bar{p}, (\bar{\rho}\tilde{E} + \bar{p})\widetilde{w}\}$$

viscous fluxes can be written as:

$$F_v = \begin{bmatrix} 0 \\ \mu_e\left\{2L_1[\tilde{u}] - \frac{2}{3}(L_1[\tilde{u}] + L_2[\tilde{v}] + L_3[\widetilde{w}])\right\} \\ \mu_e(L_1[\tilde{v}] + L_2[\tilde{u}]) \\ \mu_e(L_1[\widetilde{w}] + L_3[\tilde{u}]) \\ \tilde{u}F_{v2} + \tilde{v}F_{v3} + \widetilde{w}F_{v4} + \lambda L_1[\tilde{T}] + \frac{\bar{\rho}\nu_t}{Pr_t}L_1[\tilde{H}] \end{bmatrix} \quad (4)$$

$$G_v = \begin{bmatrix} 0 \\ \mu_e(L_1[\tilde{v}] + L_2[\tilde{u}]) \\ \mu_e\left\{2L_2[\tilde{v}] - \frac{2}{3}(L_1[\tilde{u}] + L_2[\tilde{v}] + L_3[\widetilde{w}])\right\} \\ \mu_e(L_2[\widetilde{w}] + L_3[\tilde{v}]) \\ \tilde{u}G_{v2} + \tilde{v}G_{v3} + \widetilde{w}G_{v4} + \lambda L_2[\tilde{T}] + \frac{\bar{\rho}\nu_t}{Pr_t}L_2[\tilde{H}] \end{bmatrix} \quad (5)$$

$$H_v = \begin{bmatrix} 0 \\ \mu_e(L_1[\widetilde{w}] + L_3[\tilde{u}]) \\ \mu_e(L_2[\widetilde{w}] + L_3[\tilde{v}]) \\ \mu_e\left\{2L_3[\widetilde{w}] - \frac{2}{3}(L_1[\tilde{u}] + L_2[\tilde{v}] + L_3[\widetilde{w}])\right\} \\ \tilde{u}H_{v2} + \tilde{v}H_{v3} + \widetilde{w}H_{v4} + \lambda L_3[\tilde{T}] + \frac{\bar{\rho}\nu_t}{Pr_t}L_3[\tilde{H}] \end{bmatrix} \quad (6)$$

In the above equations, $\tilde{u}$, $\tilde{v}$, $\widetilde{w}$ and $\widetilde{T}$ indicate the Favre-filtered velocity components and temperature, respectively. λ, ν_t, Pr_t represent the thermal conductivity, sub-grid viscosity, and sub-grid Prandtl number, respectively. The filtered pressure and density are denoted by $\bar{p}$ and $\bar{\rho}$, respectively. F_{vn}, G_{vn}, and H_{vn} indicate nth components of viscous flux vectors. $\tilde{e}$ indicates Favre filtered total energy and μ_e denotes the effective sub-grid dynamic viscosity. The sub-grid kinematic viscosity (ν_t) is calculated by the wall-adapted local eddy-viscosity (WALE) model [31]. $H_{ij}^{SGS}$is the sub-grid total enthalpy flux which can be modeled by using the gradient-diffusion model as follows [14,32]:

$$H_{ij}^{sgs} = -(\bar{\rho}\nu_t/Pr_t)\left(\partial\tilde{H}/\partial x_i\right). \quad (7)$$
$$\tilde{H} = \tilde{E} + \bar{p}/\bar{\rho}$$

All sub-grid terms have been represented in generalized coordinates [Eqs. (4-6)]. The Eulerian set of the Favre-filtered LES equations are solved by using a fourth-order finite-difference methodology. The spatial derivatives are obtained by using a compact-differencing fourth-order scheme [33] and [34]. The time integration is performed by using a three-stage strong, stability-preserving Runge–Kutta methodology [35]. The perturbations created by arising the numerical errors at very high frequencies is eliminated by applying a high-order spatial implicit filtering.

2.2 The filtered mass density function (FMDF)

The modeled governing transport equation for the scalar filtered mass density function can be written as [30]

$$\frac{\partial F_L}{\partial t} + \frac{\partial[\tilde{u}_i F_L]}{\partial x_i} = \frac{\partial}{\partial t}\left[(\gamma + \gamma_t)\frac{\partial(\frac{F_L}{\rho})}{\partial x_i}\right] + \frac{\partial}{\partial \psi_\alpha}\left[\Omega_m\left(\psi_\alpha - \tilde{\phi}_\alpha\right)F_L\right] - \frac{\partial\left[\hat{S}_\alpha F_L\right]}{\partial \psi_\alpha} \quad (8)$$

All information dealing with the scalar field, i.e., species concentrations and temperature, is provided by solving this equation. In the preceding equation,ϕ_α, ψ_α and Ω_m denote the scalar array, composition domain of the scalar array, and the frequency of mixing within the sub-grid, respectively. The flow field variables (including velocity and pressure) in Eq. (8) are not known and can be calculated by solving Favre-filtered LES equations via an Eulerian finite difference (FD) scheme. FMDF equation (Eq. (8)) is solved by using a Lagrangian Monte-Carlo (MC) method. In such a methodology, each MC particle is transported in physical space due to filtered velocity plus the combined effects of molecular and sub-grid diffusivities, according to the following equation (SDE) [36]:

$$dX_i(t) = \left(\tilde{u}_i + \frac{1}{\bar{\rho}}\frac{\partial(\gamma + \gamma_t)}{\partial x_i}\right)dt + \sqrt{2\,(\gamma + \gamma_t)/\bar{\rho}}\,dW_i(t) \quad (9)$$

where X_i denotes the physical location of the MC particle, and W_i is the Wiener process

[37]. Each MC particle contains information on scalar variables, including species concentrations and temperature. This information can be updated due to mixing and chemical reaction according to the following equation:

$$\frac{d\phi_\alpha^+}{dt} = -C_\Omega \frac{\gamma+\gamma_t}{\bar{\rho}}(\phi_\alpha^+ - \tilde{\phi}_\alpha) + \hat{S}_\alpha(\phi^+) \quad (10)$$

where $\phi_\alpha^+ = \phi_\alpha(X(t).t)$ is the scalar variable describing each MC particle with the Lagrangian location vector X_i. The MC particle n contains information on its location,$x^n(t)$, velocity, $u^n(t)$, and scalar variable, $\phi^n(t)$, $n = 1.2.\ldots.N_p$. The integration of SDE ($dx = Ddt + EdW$) can be performed using the Euler–Maruyama approximation [38], which yields to the following equation:

$$x_i^n(t_{k+1}) = x_i^n(t_k) + D_i^n(t_k)\Delta t + E^n(t_k)(\Delta t)^{1/2}\xi_i^n(t_k).\ i = 1.2.3 \quad (11)$$

where $\xi_i^n(t_k)$ are independent standardized Gaussian random variables. For more information about LES/FMDF methodology and its implementation schemes, readers can refer to [25] and [30].

In the hybrid LES/FMDF methodology, filtered velocity components are determined by resolving LES governing equations and are utilized in the FMDF equation. However, chemical source terms are provided by Lagrangian FMDF solver. The fuel mass fraction and temperature scalars can be calculated by solving the FMDF equation, and it is not mandatory to solve a conservative Eulerian equation to obtain the scalar field. However, the consistency between the Lagrangian and Eulerian methods is indicated by resolving the scalar field via an Eulerian conserved scalar equation in which the chemical source term comes from Lagrangian FMDF solver.

3. Results

The utilized numerical scheme and flow solver have been verified by carrying out large-eddy simulations of various reacting and non-reacting flows, including internal combustion engines, round/planar turbulent jets, isotropic turbulence, jet in crossflows and turbulent flow in dump combustors [26–29,39–41]. In the present study, this verified flow solver is utilized to simulate propane turbulent combustion in a single-cavity trapped-vortex combustor.

3.1. Geometry, mesh, and boundary conditions

This paper's emphasis is on the investigation of turbulent flows in a planar trapped-vortex combustor via large-eddy simulation. A commonly used geometry for planar TVCs with one cavity is considered in this study, as shown in Fig. 1. The cavity aspect ratio (L/D) is set to be unity as it leads to stable combustion, lower pressure losses, and acceptable exit temperature pattern factor [42,43]. A gaseous propane jet and an air jet are injected from cavity forebody and afterbody, respectively. A mixture consisted

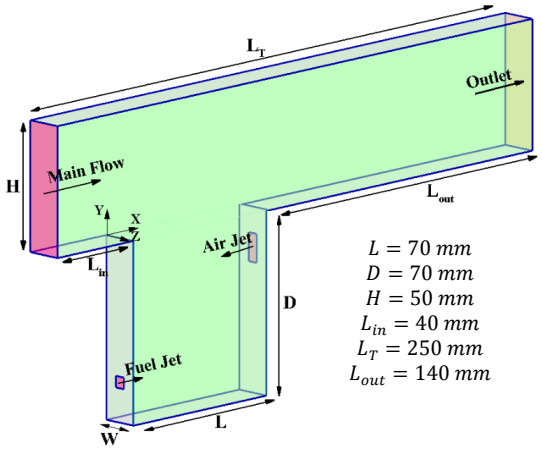

(a)

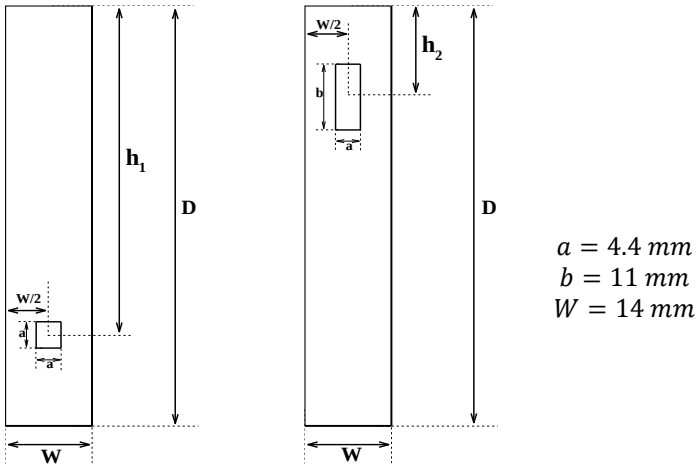

(b)

Fig. 1 (a) Geometry and dimensions of the considered typical trapped vortex, (b) Fuel jet entrance geometry on the cavity forebody (left) and air jet entrance geometry on the cavity afterbody (right)

of propane and air with an equivalence ratio of 0.15 is entering as the main flow. Based on the air and fuel jet velocities, the cavity and the overall equivalence ratios are 1.85 and 0.44, respectively. Five configurations of fuel and air jet positions are considered. The main objective of the present study is to compare the combustion characteristics of different configurations of fuel and air injection. Temperature field, flame shape, and combustion efficiency are invoked to accomplish this.

A simple global-chemical-kinetics model is invoked to simulating turbulent reacting flow with pure propane combustion, according to Eq. (12). The reaction rate for this mechanism is represented in the Arrhenius form [44].

$$C_3H_8 + 5(O_2 + 3.76N_2) \longrightarrow 3CO_2 + 4H_2O + 18.8N_2 \quad (12)$$

At inlets, a characteristic inflow boundary condition is applied, and a perturbed velocity with a flat mean profile is imposed. Velocity magnitude, temperature, and fuel mass fraction for air/fuel injections are given in Table 2. The walls are treated as adiabatic no-slip boundaries. A characteristic boundary condition is applied at the outlet. A periodic boundary condition is employed on the side boundaries, i.e., the flow is assumed to be repeatable in the transverse direction.

3.2. Grid resolution

The computational domain is covered by a multi-block structured mesh that is clustered in high gradient regions, near solid walls and shear layers. The blocks can exchange their flow information through common boundaries between the blocks. For the reference grid layout, the smallest grid size is

Table 1. Fuel and air jet relative positions

Configuration No.	$h_1(mm)$	$h_2(mm)$
1	55	15
2	15	55
3	35	35
4	15	15
5	55	55

Table 2. Inlet parameters for mainstream, fuel jet and air jet inlets

Boundary	Reynolds number	Velocity (m/s)	Temperature (K)	Fuel mass fraction
Mainstream inlet	29000	8.4	500	0.01
Fuel Jet Inlet	2200	7.1	500	1.00
Air Jet Inlet	10200	23.6	500	0.00

is $0.3\,mm$ in all three Cartesian directions, and the largest is 5 times larger. The results with various grid resolutions show very slight discrepancies in the solution vector.

The resolution of the reference computational grid which the results are presented for is also evaluated by using the Pope criterion [45], that is at least 80% of turbulence kinetic energy be resolved in the grid nodes, meaning only up to 20% of the kinetic turbulence energy must be modeled. In other words, the turbulent resolution that is given by Eq. (13), must be less than 0.2.

$$M_{pope} = \frac{k_{sgs}}{k_{sgs} + k_{res}}, \qquad (13)$$

$$k_{res} = \frac{1}{2}\langle u_i' u_i' \rangle$$

k_{res} and k_{sgs} are the resolved and modeled portions of turbulence kinetic energy. In this equation, the sub-grid kinetic energy is given [45]:

$$k_{sgs} = \frac{\langle v_t^2 \rangle}{\left(\sqrt{\frac{2}{3}}\frac{A}{\pi K_0^{2/3}}\Delta\right)^2}, \qquad (14)$$

$$A = 0.44, \qquad K_0 = 1.4$$

The nodes distribution over "turbulence resolution" for configuration 1 is given in Fig.2 It can be seen that the turbulence resolution in the entire domain hasa value of less than 0.2. Consequently, the mesh is suitable for our LES calculations.

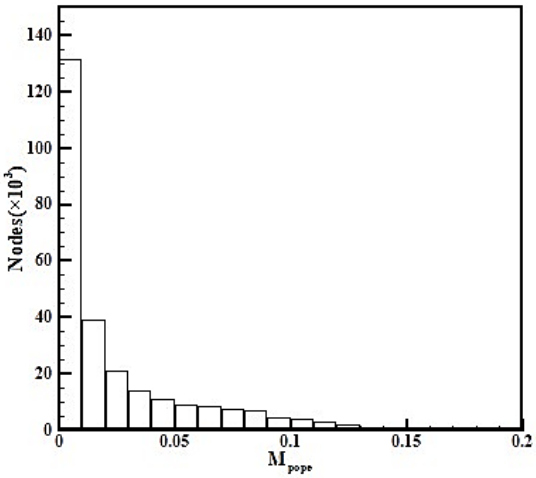

Fig.2. The nodes distribution over turbulence resolution for configuration 1.

3.3. Temperature consistency

As discussed in section 2.2, in LES/FMDF methodology, the fuel species conservation equation and energy equation are resolved in both Eulerian finite-difference and Lagrangian Monte Carlo schemes and the results obtained by two schemes must be consistent. A horizontal section on the center-plane of the cavity at $\frac{y}{D} = -\frac{1}{2}$ is considered in order to plot temperature profiles and evaluate consistency. The instantaneous and time-averaged temperature distributions obtained from FD and MC schemes indicate an acceptable consistency between the two solvers in Fig.3.

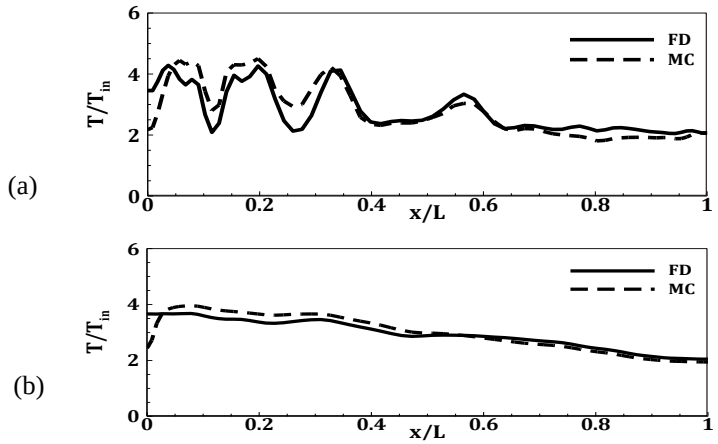

Fig.3. Temperature distribution on the cavity center-plane at $\frac{y}{D} = -\frac{1}{2}$ for configuration 1
(a) instantaneous values, (b) time-averaged values

The temperature contours can also be used to evaluate the consistency. The instantaneous and time-averaged temperature contours of case 5 for both FD and MC solvers are shown in Fig.4. As expected, good consistency can be seen between FD and MC schemes.

3.4. The flow and temperature field

Investigation of the flow field is valuable due to its considerable effects on the flame structure and temperature distribution. Flow characteristics, including velocity contours and streamlines representing the vortical structure, are invoked to establish an insightful perception of the flow field and its impacts on the mixing and combustion inside the combustor. Figure 5 shows the longitudinal velocity normalized by inlet bulk velocity for case 1 at the TVC center-plane. Velocities up to 8 times mainstream inlet velocity are created due to chemical reaction and heat release. The flame is formed around the fuel jet, accompanied by a volume expansion which causes the flow to accelerate at the vicinity of the fuel jet.

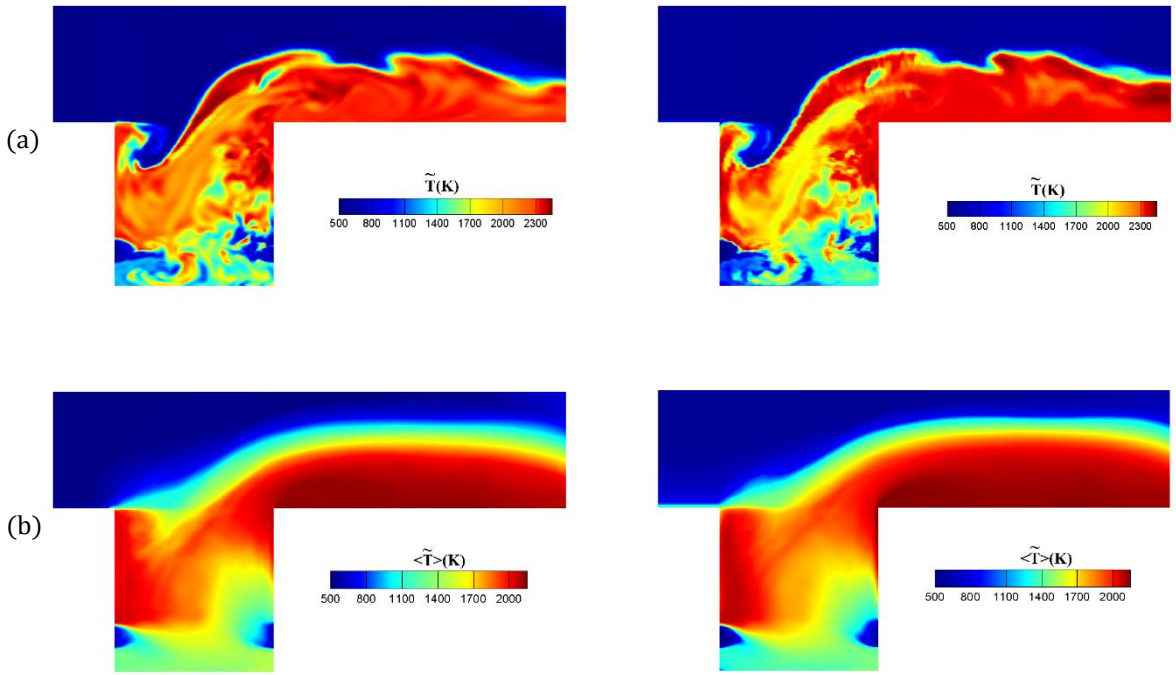

Fig.4. Temperature field for case 5 on the TVC center-plane obtained by MC scheme (right) and FD scheme (left), (a) Instantaneous field, (b) Time-averaged field

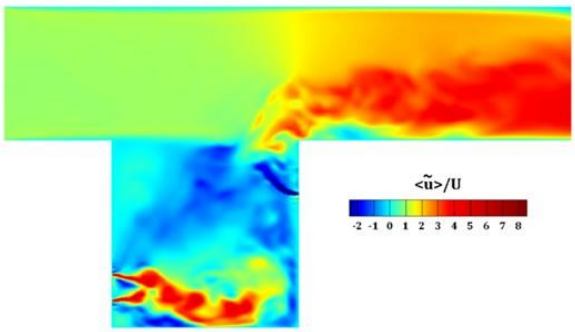

Fig.5. Normalized instantaneous longitudinal velocity at the TVC center-plane for configuration 1

The temperature field and maximum flame temperature are among the crucial features of any combustor. A more uniform temperature distribution provides complete combustion and hence, less CO and soot production. Also, a higher flame temperature results in high levels of NOx emission.

Figure 6 depicts temperature distribution along with time-averaged streamlines on the TVC center-plane for all configurations. Configurations 1 and 2 have a relatively non-uniform temperature distribution, as the hot gases are trapped inside a vortex and 'don't spread throughout the cavity, which disrupts the ignition of inlet fuel and air. In case 1, a vortex created by flow separation near the cavity leading edge recirculates the hot gases within the cavity, while in case 2, a vortex steered by air jet does the same. Configurations 3, 4, and 5 establish relatively a more uniform temperature field since hot gases are well-distributed by the vortical structures, which implies that a better mixing occurred in these three cases.

The maximum flame temperature for every configuration, is identified in the contour legend. Configuration 3 with a maximum temperature by 2007 K and configuration 4 with a maximum temperature by 2353 K establish the lowest and highest maximum temperatures, respectively. Configuration 5 is in the second rank from the standpoint of the lowest maximum temperature. Configurations 1 and 2 also have a relatively high maximum temperature. The maximum temperature for cases 1, 3, 4, and 5 occurs at the recirculation zone created right after the trailing edge of the cavity. That is because a recirculation zone after the trailing edge generates a stationary hot region. For case 2, such a recirculation zone 'isn't created, and the maximum temperature occurs at the center of the main vortex formed within the cavity.

Configuration 1

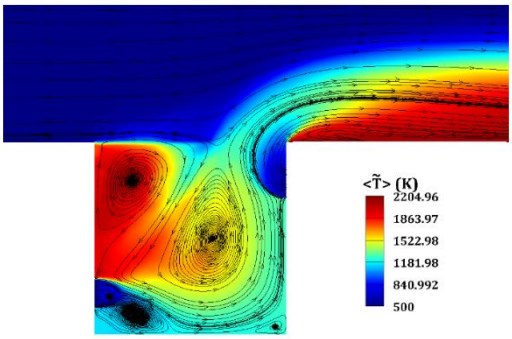

Configuration 2

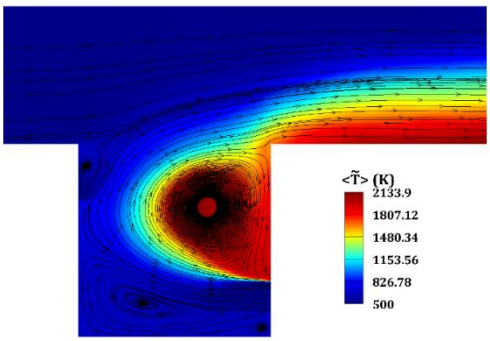

Configuration 3

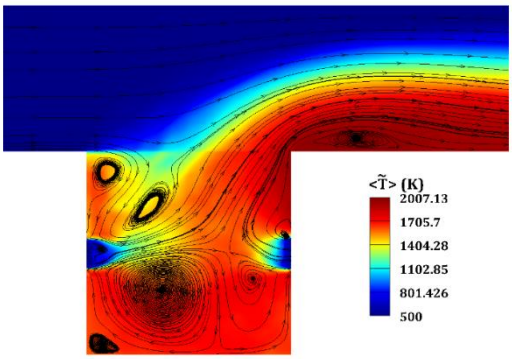

Configuration 4

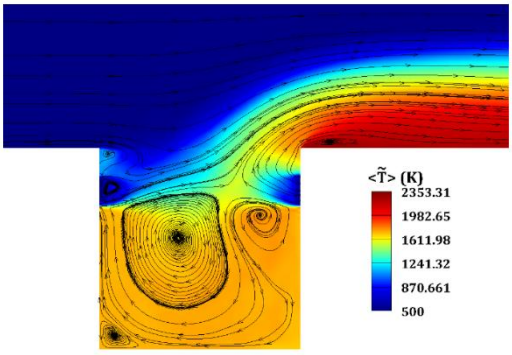

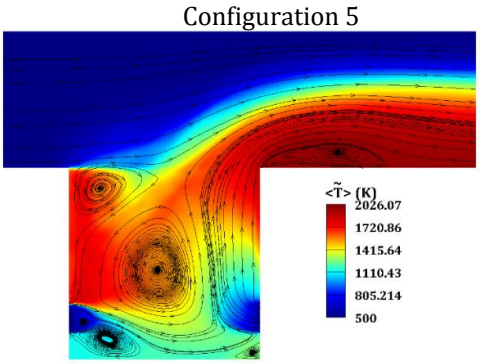

Fig.6. Mean flow streamlines together with the time-averaged temperature field

For further investigation of temperature distribution, one can utilize a cross-sectional averaged temperature. Figure 7 shows the cross-sectional mean temperature profiles versus axial location. Adiabatic flame temperature (T_{ad}) based on the overall equivalence ratio is 1556 K, which is identified by a horizontal dashed line in the figure. As expected, configurations 1 and 2, which have the most non-uniform temperature distribution inside the cavity, provide the farthest mean temperature curves to T_{ad}. By contrast, configuration 3 and 4 provide the closest mean temperature curves to T_{ad} within the cavity. Among these two configurations, case 4 has a lower mean temperature. The mean temperature for case 5 is slightly lower than cases 3 and 4 in the cavity but with a more uniform distribution. Based on this examination, configuration 4 could be considered as the most favorable configuration.

3.5. Flame structure

Reaction rate distribution is a common tool to identify approximate flame shape and location. The formation of a short and well-contained flame inside the cavity is desirable for any trapped vortex combustor. Due to the rich nature of fuel-air mixture within the cavity, the reaction rate distribution is more intense everywhere at which there is enough air, such as regions close to air jet. Figure 8 shows the instantaneous and time-averaged reaction rate distributions for all configurations discussed in this paper.

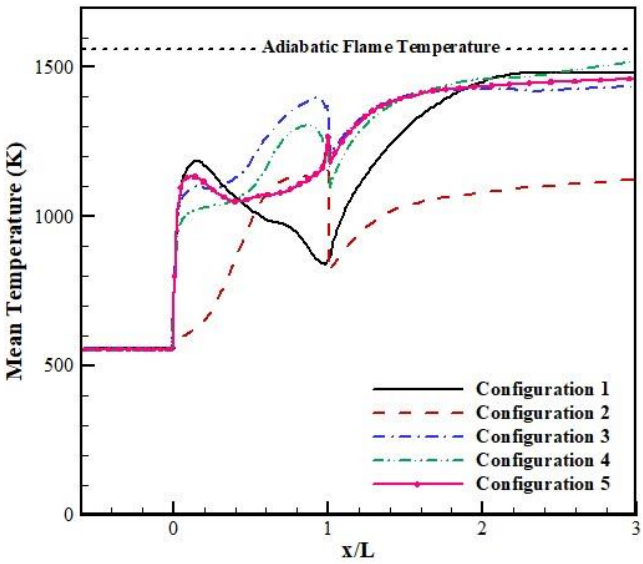

Fig.7. Longitudinal variation of cross-sectional averaged temperature for all configurations

In case 1, the major part of the flame is present in the outlet channel, and the small part is an undistributed flame that is localized in the cavity upstream half. Referring to the flow field, the flame located inside the cavity is created by the reaction of the fuel injected and mainstream entrained into the cavity. However, the flame anchored in the outlet channel is formed by the reaction of cavity fuel and mainstream/cavity air. Thereby, case 1 'doesn't provide good performance in flame stabilization inside the cavity, which is the main function of cavity flame-holder. The flame in case 2 is a weak flame located in the downstream half of the cavity and lower half of the outlet channel. Poor mixing between fuel and air, in this case, results in a flame with a non-uniform temperature distribution. Case 3 has a larger flame length but contains the flame inside the cavity better than two previous cases. In this case, the flame is mainly established in the cavity upper half due to the injection of the fuel and air from midpoints. The flame is more intense in the cavity right half, so there is a higher cross-sectional averaged temperature in this region, as shown in Fig.7.

In case 4, the whole flame is created closer to the mainstream and outlet channel as the injection points are close to the mainstream. The establishment of a zone with an intense reaction rate air jet's proximity, leads to an increase in cross-sectional averaged temperature. Case 5 provides a relatively short and well-contained flame inside the cavity. The cases 4 and 5 provide flames with approximately equal lengths, which are shorter than cases 1, 2, and 3; however, in case 5, the flame is better positioned inside the cavity.

Case 1:

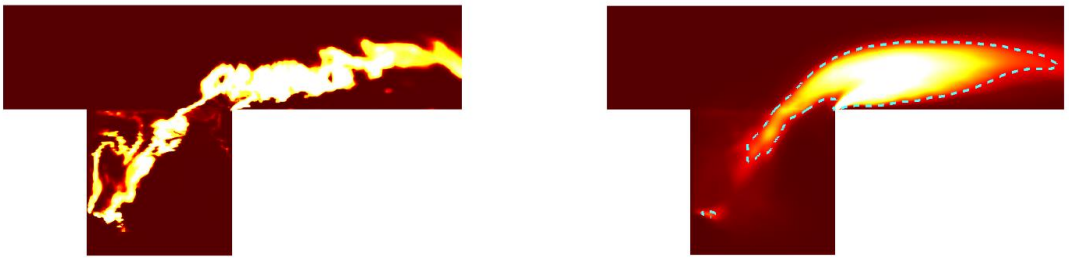

Case 2:

Case 3:

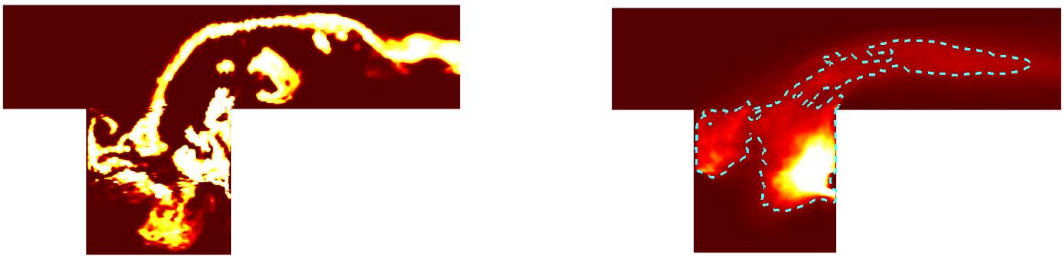

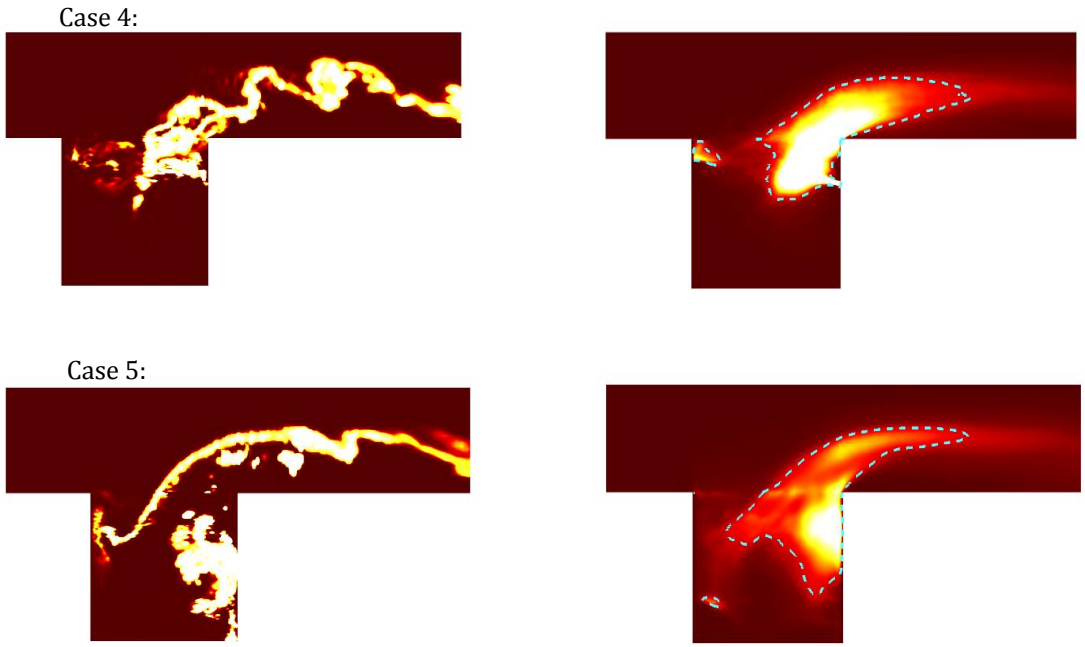

Fig.8. instantaneous reaction rate (left) and time-averaged reaction rate with an approximate flame location (right)

4. Conclusions

Turbulent combustion of gaseous propane in a planar single-cavity TVC with a fuel jet on the forebody and an air jet on the afterbody of the cavity was computationally investigated using the LES/FMDF methodology. Different injection schemes were contemplated by altering fuel and air jet locations representing the different flow and flame structures. The temperature distribution, along with flame structure, was invoked for combustion characterization of different injection strategies. The numerical results revealed that configurations in which both air and fuel jets are located at the cavity-walls midpoint or adjacent to the cavity inferior wall, lead to a more contained flame and low maximum temperature, with the latter configuration performing slightly better while the former configuration provides the closest cross-sectional averaged temperature to the adiabatic flame temperature.

References

[1] K. Hsu, L. Gross, D.D. Trump, W.M. Roquemore, Performance of a trapped-vortex combustor, in: 33rd Aerosp. Sci. Meet. Exhib., 1995: p. 810.

[2] R.C. Hendricks, D.T. Shouse, W.M. Roquemore, D.L. Burrus, B.S. Duncan, R.C. Ryder, A. Brankovic, N.-S.N.-S. Liu, J.R. Gallagher, W.M. Roquernore, D.L. Burrus, B.S. Duncan, R.C. Ryder, A. Brankovic, N.-S.N.-S. Liu, J.R. Gallagher, J.A. Hendricks, Experimental and computational study of trapped vortex combustor sector rig with tri-pass diffuser, (2004).

[3] R.C. Hendricks, D.T. Shouse, W.M. Roquemore, D.L. Burrus, B.S. Duncan, R.C. Ryder, A. Brankovic, N.-S. Liu, J.R. Gallagher, J.A. Hendricks, Experimental and computational study of trapped vortex combustor sector rig with high-speed diffuser flow, Int. J. Rotating Mach. 7 (2001) 375–385.

[4] G. Sturgess, K.-Y. Hsu, Entrainment of mainstream flow in a trapped-vortex combustor, in: 35th Aerosp. Sci. Meet. Exhib., 1997: p. 261. doi:10.2514/6.1997-261.

[5] K.-Y. Hsu, L.P. Goss, W.M. Roquemore, Characteristics of a trapped-vortex

combustor, J. Propuls. Power. 14 (1998) 57–65.

[6] Z. Rongchun, F. Weijun, Flow field measurements in the cavity of a trapped vortex combustor using PIV, J. Therm. Sci. 21 (2012) 359–367. doi:10.1007/s11630-012-0556-z.

[7] Z. Wu, Y. Jin, X. He, C. Xue, L. Hong, Experimental and numerical studies on a trapped vortex combustor with different struts width, Appl. Therm. Eng. 91 (2015) 91–104. doi:10.1016/j.applthermaleng.2015.06.068.

[8] S. Krishna, R. V. Ravikrishna, Optical diagnostics of fuel-air mixing and vortex formation in a cavity combustor, Exp. Therm. Fluid Sci. 61 (2015) 163–176. doi:10.1016/j.expthermflusci.2014.10.012.

[9] D.L. Blunck, D.T. Shouse, C. Neuroth, A. Lynch, T.J. Erdmann, D.L. Burrus, J. Zelina, D. Richardson, A. Caswell, Experimental Studies of Cavity and Core Flow Interactions With Application to Ultra-Compact Combustors, J. Eng. Gas Turbines Power. 136 (2014) 091505. doi:10.1115/1.4026975.

[10] D.L. Straub, K.H. Casleton, R.E. Lewis, T.G. Sidwell, D.J. Maloney, G.A. Richards, Assessment of Rich-Burn, Quick-Mix, Lean-Burn Trapped Vortex Combustor for Stationary Gas Turbines, J. Eng. Gas Turbines Power. 127 (2005) 36. doi:10.1115/1.1789152.

[11] P.K. Ezhil Kumar, D.P. Mishra, Combustion Characteristics of a Two-Dimensional Twin Cavity Trapped Vortex Combustor, J. Eng. Gas Turbines Power. 139 (2017) 71504–71510. http://dx.doi.org/10.1115/1.4035739.

[12] V. Katta, W.M. Roquemore, Numerical studies of trapped-vortex combustor, in: 32nd Jt. Propuls. Conf. Exhib., 1996: p. 2660.

[13] D.P. Mishra, R. Sudharshan, Numerical analysis of fuel-air mixing in a two-dimensional trapped vortex combustor, Proc. Inst. Mech. Eng. Part G J. Aerosp. Eng. 224 (2010) 65–75. doi:10.1243/09544100JAERO535.

[14] C. Stone, S. Menon, Simulation of fuel-air mixing and combustion in a trapped-vortex combustor, in: 38th Aerosp. Sci. Meet. Exhib., 2000: p. 478.

[15] Z. Zeng, J. Ren, X. Liu, Z. Xu, The unsteady turbulence flow of cold and combustion case in different trapped vortex combustor, Appl. Therm. Eng. 90 (2015) 722–732. doi:10.1016/j.applthermaleng.2015.07.041.

[16] S. Chen, R.S.M. Chue, J. Schlüter, T.T.Q. Nguyen, S.C.M. Yu, Numerical Investigation of a Trapped Vortex Miniature Ramjet Combustor, J. Propuls. Power. 31 (2015) 872–882. doi:10.2514/1.B35602.

[17] S. Krishna, R. V. Ravikrishna, Numerical and Experimental Studies on a Syngas-Fired Ultra Low NO_x Combustor, J. Eng. Gas Turbines Power. 139 (2017) 111502. doi:10.1115/1.4036945.

[18] Y. Jin, X. He, J. Zhang, B. Jiang, Z. Wu, Numerical investigation on flow structures of a laboratory-scale trapped vortex combustor, Appl. Therm. Eng. 66 (2014) 318–327. doi:10.1016/j.applthermaleng.2014.02.030.

[19] P.K. Ezhil Kumar, D.P. Mishra, Numerical study of reacting flow characteristics of a 2D twin cavity trapped vortex combustor, Combust. Theory Model. 21 (2017) 658–676. doi:10.1080/13647830.2017.1281441.

[20] M. Li, X. He, Y. Zhao, Y. Jin, Z. Ge, W. Huang, Effect of strut length on combustion performance of a trapped vortex combustor, Aerosp. Sci. Technol. 76 (2018) 204–216. doi:10.1016/j.ast.2018.02.019.

[21] K.M. Zbeeb, T.T. Dimensional, T.T. Dimensional, C. Molecule, C. Monoxide, C. Dioxide, C.F. Dynamics, Fuel Injector Reynolds Number Effects on Performance and Emissions of a Trapped Vortex Combustor, in: 23rd AIAA Comput. Fluid Dyn. Conf., 2017: p. 3794. doi:10.2514/6.2017-3794.

[22] Y.-Y. Liu, R.-M. Li, H.-X. Liu, M.-L. Yang, Effects of Fueling Scheme on the Performance of a Trapped Vortex

Combustor Rig, in: 45th AIAA/ASME/SAE/ASEE Jt. Propuls. Conf. Exhib., 2009: p. 4831.

[23] D. Zhao, E. Gutmark, P. de Goey, A review of cavity-based trapped vortex, ultra-compact, high-g, inter-turbine combustors, Prog. Energy Combust. Sci. 66 (2018) 42–82. doi:10.1016/j.pecs.2017.12.001.

[24] S.L. Yilmaz, N. Ansari, P.H. Pisciuneri, M.B. Nik, C.C. Otis, P. Givi, Applied Filtered Density Function., J. Appl. Fluid Mech. 6 (2013).

[25] A. Afshari, F.A. Jaberi, T.I.P. Shih, Large-eddy simulations of turbulent flows in an axisymmetric dump combustor, AIAA J. 46 (2008) 1576–1592.

[26] A. Afshari, F.A. Jaberi, Large-scale simulations of turbulent combustion and propulsion systems, Combust. Process. Propuls. Control. Noise, Pulse Detonation. (2006) 31.

[27] M. Esmaeili, A. Afshari, F.A. Jaberi, Large-eddy simulation of turbulent mixing of a jet in crossflow, J. Eng. Gas Turbines Power. 137 (2015) 91510.

[28] M. Esmaeili, A. Afshari, F.A. Jaberi, Turbulent mixing in non-isothermal jet in crossflow, Int. J. Heat Mass Transf. 89 (2015) 1239–1257.

[29] P. Givi, Filtered density function for subgrid scale modeling of turbulent combustion, AIAA J. 44 (2006) 16–23.

[30] F.A. Jaberi, P.J. Colucci, S. James, P. Givi, S.B. Pope, Filtered mass density function for large-eddy simulation of turbulent reacting flows, J. Fluid Mech. 401 (1999) 85–121.

[31] F. Nicoud, F. Ducros, Subgrid-scale stress modelling based on the square of the velocity gradient tensor, Flow, Turbul. Combust. 62 (1999) 183–200. doi:10.1023/A:1009995426001.

[32] W.-W. Kim, S. Menon, Les of turbulent fuel/air mixing in a swirling combustor, in: 37th Aerosp. Sci. Meet. Exhib., 1998: p. 200.

[33] S.K. Lele, Compact finite difference schemes with spectral-like resolution, J. Comput. Phys. 103 (1992) 16–42.

[34] M.R. Visbal, D. V Gaitonde, Very high-order spatially implicit schemes for computational acoustics on curvilinear meshes, J. Comput. Acoust. 9 (2001) 1259–1286.

[35] S. Gottlieb, C.-W. Shu, E. Tadmor, Strong stability-preserving high-order time discretization methods, SIAM Rev. 43 (2001) 89–112.

[36] C.W. Gardiner, Handbook of stochastic methods volume 13 of the Springer series in synergetics, J. Opt. Soc. Am. B Opt. Phys. 1 (n.d.) 409.

[37] S. Karlin, H.E. Taylor, A second course in stochastic processes, Elsevier, 1981.

[38] P.E. Kloeden, E. Platen, H. Schurz, Stochastic differential equations, in: Numer. Solut. SDE Through Comput. Exp., Springer, 1994: pp. 63–90.

[39] J. Kim, A. Afshari, D. Bodony, J. Freund, LES investigation of a Mach 1.3 jet with and without plasma actuators, in: 47th AIAA Aerosp. Sci. Meet. Incl. New Horizons Forum Aerosp. Expo., 2009: p. 290.

[40] A. Banaeizadeh, A. Afshari, H. Schock, F. Jaberi, Large eddy simulations of turbulent flows in IC engines, in: ASME 2008 Int. Des. Eng. Tech. Conf. Comput. Inf. Eng. Conf., American Society of Mechanical Engineers, 2008: pp. 399–407.

[41] M.R.H. Sheikhi, T.G. Drozda, P. Givi, F.A. Jaberi, S.B. Pope, Large eddy simulation of a turbulent nonpremixed piloted methane jet flame (Sandia Flame D), Proc. Combust. Inst. 30 (2005) 549–556.

[42] K.K. Agarwal, R. V. Ravikrishna, Experimental and numerical studies in a compact trapped vortex combustor: Stability assessment and augmentation, Combust. Sci. Technol. 183 (2011) 1308–1327. doi:10.1080/00102202.2011.592516.

[43] K.K. Agarwal, R. V. Ravikrishna, Flow-acoustic Characterisation of a Cavity-based Combustor Configuration, Def. Sci. J. 61 (2011) 523–528. doi:10.14429/dsj.61.870.

[44] H. Yu, L.-S. Luo, S.S. Girimaji, Scalar mixing and chemical reaction simulations using lattice Boltzmann method, Int. J. Comput. Eng. Sci. 3 (2002) 73–87.

[45] S.B. Pope, Turbulent flows, IOP Publishing, 2001.